

# Improved spectral models for relativistic reflection

Andrzej Niedźwiecki,<sup>1</sup>\* Michał Szanecki<sup>2</sup>\* and Andrzej A. Zdziarski<sup>2</sup>\*

<sup>1</sup>*Department of Astrophysics, Łódź University, Pomorska 149/153, 90-236 Łódź, Poland*

<sup>2</sup>*Nicolaus Copernicus Astronomical Center, Polish Academy of Sciences, Bartycka 18, PL-00-716 Warszawa, Poland*

17 May 2018

## ABSTRACT

We have developed improved spectral models of relativistic reflection in the lamppost and disc-corona geometries. The models calculate photon transfer in the Kerr metric and give the observed photon-energy spectra produced by either thermal Comptonization or an e-folded power law incident on a cold ionized disc. Radiative processes in the primary X-ray source and in the disc are described with the currently most precise available models. Our implementation of the lamppost geometry takes into account the presence of primary sources on both sides of the disc, which is important when the disc is truncated. We thoroughly discuss the differences between our models and the previous ones. An application of our lamppost model to X-ray data for the Seyfert galaxy NGC 4151 disfavors the geometry of a disc extending close to the innermost stable circular orbit irradiated by a primary source close to the horizon.

**Key words:** accretion, accretion discs – black hole physics – galaxies: active – galaxies: individual: NGC 4151 – X-rays: binaries.

## 1 INTRODUCTION

Accreting sources around compact objects often contain both hot, mildly relativistic, plasma and a cold medium, usually an optically-thick accretion disc. Then the emission of the hot plasma not only reaches the observer but also irradiates the cold medium. This process is usually called Compton reflection. The pioneering paper studying this process was that of [Basko, Sunyaev & Titarchuk \(1974\)](#), who considered reflection of X-rays emitted by the accretion flow from the atmosphere of the companion star in a close binary. Since then, a lot of work on this subject has been done. In particular, [White, Lightman & Zdziarski \(1988\)](#) derived angle-averaged Green’s function for reflection from a fully ionized medium, which were extended to include bound-free absorption in [Lightman & White \(1988\)](#). [Magdziarz & Zdziarski \(1995\)](#) then derived the corresponding Green’s functions dependent on the viewing angle.

However, those works treated the absorption probability as constant throughout the reflecting medium, while the ionization structure and temperature of that medium do depend on the depth from the surface. Calculations taking into account the effect of that were performed, e.g., in [Ross & Fabian \(1993, 2005, 2007\)](#). The current most comprehensive publicly available treatment of those effects (though for a constant density medium) appears to be that of [García & Kallman \(2010\)](#) and [García et al. \(2014, 2016\)](#). In the present work, we use their numerical model.

In the vicinity of black holes (BHs) and neutron stars, these

spectra are modified by relativistic effects. [Fabian et al. \(1989\)](#) gave an approximate treatment of those, considering the main X-ray feature in reflection spectra, the fluorescent Fe  $K\alpha$  line. Since then, there have been many studies of the relativistic effects in reflection, e.g., those of [Dovčiak, Karas & Yaqoob \(2004\)](#); [Dovčiak et al. \(2011\)](#) and [Dauser et al. \(2010, 2013, 2016\)](#). A popular family of `xspec` ([Arnaud 1996](#)) models, `relxill`, is based on the latter work.

The relativistic effects were treated in two main geometries. In one, the primary source of X-rays was assumed to cover an accretion disc, and emit with a prescribed radial profile. In the other, a point-like X-ray source was assumed to be located on the BH rotation axis, and irradiate a surrounding flat disc ([Martocchia & Matt 1996](#); [Miniutti & Fabian 2004](#)). Both geometries are included in the `relxill` model family. The latter has become a popular model for accreting systems in both binaries containing either a BH or a neutron star and for active galactic nuclei (e.g., [Parker et al. 2014, 2015](#); [Degenaar et al. 2015](#); [Keck et al. 2015](#); [Fürst et al. 2015](#); [Beuchert et al. 2017](#); [Basak et al. 2017](#); [Xu et al. 2018](#); [Tomsick et al. 2018](#)).

However, certain inaccuracies of the `relxill` models were found by [Niedźwiecki, Zdziarski & Szanecki \(2016\)](#). Given those, we have developed new `xspec` models for relativistic reflection. One is `reflkerr`, which computes the observed primary and reflection spectra for a broken power-law radial emissivity profile, approximating the case of a disc corona, as in the `relxill` model. Another is `reflkerr_lp`, which computes the observed primary and reflection spectra in the lamppost geometry, as in `relxilllp`. One modification with respect to the previous models is taking into account the primary sources on both sides of the

\* E-mail: niedzwiecki@uni.lodz.pl (AN), mitsza@camk.edu.pl (MS), aaz@camk.edu.pl (AAZ)

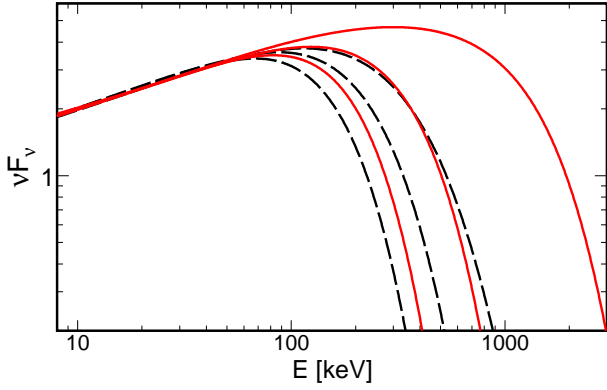


**Figure 1.** Rest-frame thermal Comptonization spectra for  $kT_{\text{bb}} = 1$  eV,  $\Gamma = 1.7$  and  $kT_e = 50, 100$  and  $400$  keV (from left to right) computed with `compps` in spherical geometry (red solid curves) and with `nthcomp` (black dashed curves). We see that `nthcomp` significantly underestimates the positions of the high-energy cutoff.

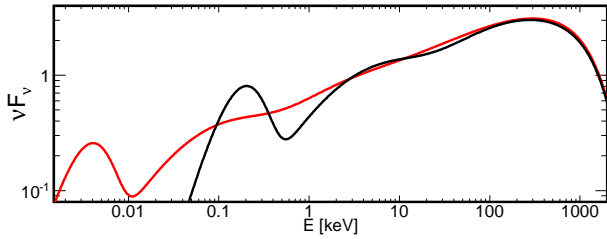


**Figure 2.** Rest-frame thermal Comptonization spectra in spherical geometry calculated with `compps` for  $kT_{\text{bb}} = 1$  eV (red curves) and  $50$  eV (black curves), at  $kT_e = 400$  keV and  $\tau = 0.32$ , yielding  $\Gamma \approx 1.7$ . We see the seed-photon blackbody spectra (slightly attenuated due to up-scattering) on the left-hand side. The first two scattering orders are clearly visible, which effect is much less visible at  $E \gtrsim 1$  keV in the case of  $kT_{\text{bb}} = 1$  eV.

accretion disc, which is important in the presence of disc truncation (Niedźwiecki & Zdziarski 2018). In this work, we present our formalism and discuss the main improvements with respect to the previous treatments. We then compare our spectra with those of `relxill` and `relxilllp`. Finally, as an example application, we fit both models to X-ray data for the Seyfert galaxy NGC 4151, and show the resulting differences.

## 2 THE INCIDENT SPECTRUM

We choose Comptonization of soft blackbody photons by mildly relativistic thermal electrons as the physical incident spectrum in the rest frame. This process appears to be the dominant one in coronae in the vicinity of inner accretion discs in X-ray binaries (e.g., Zdziarski & Gierliński 2004; Done, Gierliński & Kubota 2007; Burke, Gilfanov & Sunyaev 2017 and references therein). The accuracy of hard X-ray/soft  $\gamma$ -ray spectra measured from Seyferts and radio galaxies is lower than that for X-ray binaries. Still, high-energy cutoffs compatible with thermal Comptonization are commonly observed, e.g., Madejski et al. (1995), Zdziarski, Johnson & Magdziarz (1996), Gondek et al. (1996), Zdziarski, Poutanen & Johnson (2000), Zdziarski & Grandi (2001), Malizia et al. (2008), Marinucci et al. (2014), Brenneman et al. (2014), Ballantyne et al. (2014),

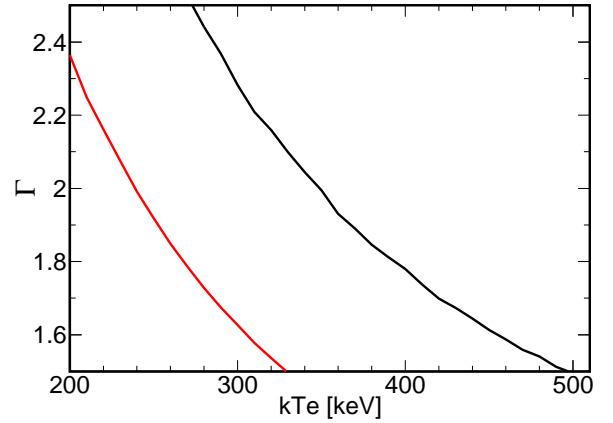


**Figure 3.** Approximate limits for a power-law shape of thermal Comptonization spectra in the spherical geometry for  $kT_{\text{bb}} = 1$  eV (black) and  $kT_{\text{bb}} = 50$  eV (red). At the electron temperatures above those given by the curves, the difference of the spectral indices fitted in the 2–5 keV and 8–15 keV ranges exceeds 0.05.

Baloković et al. (2015), Fabian et al. (2015), Lubiński et al. (2016).

In order to reproduce this spectrum, we use the `compps` model (Poutanen & Svensson 1996), which gives an excellent agreement with our Monte Carlo simulations for any set of thermal plasma parameters with the Thomson optical depth of  $\tau \lesssim 3$ . That model allows a choice of the plasma geometry and the distribution of seed photons. In the case of the coronal geometry, with a corona above a disc, our model of relativistic effects, `reflkerr`, assumes a slab plasma geometry. In the case of the lamppost source, our relativistic model, `reflkerr_lp`, assumes a spherical plasma geometry.

The model parameters of thermal Comptonization are the optical depth,  $\tau$  (measured from either the bottom of a slab or the centre of a sphere), the electron temperature,  $T_e$ , and the blackbody seed photons temperature,  $T_{\text{bb}}$ . The X-ray photon spectral index,  $\Gamma$  [ $N(E) \propto E^{-\Gamma}$ ], is approximately determined by the product of  $T_e$  and  $\tau$ . The user can choose between various versions of either spherical or slab geometry available in `compps` by setting the geometry parameter, which determines the shape of the scattering plasma and the spatial distribution of seed photons. This parameter has the same meaning as in `compps`. In the case of coronal geometry, in the `reflkerr` model, the user can choose 1 for slab geometry with the seed photons emitted from the bottom of the slab with a constant specific intensity (default) and  $-1$  for isotropic and homogeneous seed photons. In the lamppost case (`reflkerr_lp`), the choices are 4 for a sphere with seed photons emitted from the centre and  $-4$  for homogeneous seed photon distribution, and  $-5$  for isotropic seed photons distributed radially along  $\tau'$  proportional to  $\sin(\pi\tau'/\tau)/(\pi\tau'/\tau)$ , and 0 using a fast approximate method based on escape probability from a sphere (default).

We note that `compps` is the most accurate thermal Comptonization model currently implemented in `xspec`. The model `nthcomp` (Zdziarski et al. 1996), which is used in `relxilllpCp`, correctly approximates the Comptonization spectrum only for  $\tau \gtrsim 1$  and it strongly underestimates the high-energy extent of the spectrum for  $kT_e \gtrsim 100$  keV, see Fig. 1. This is a crucial shortcoming for lamppost models with a low height above the horizon, where we would not be able to properly model the observed spectra extending up to  $\sim 100$  keV in the rest-frame with `nthcomp` when the

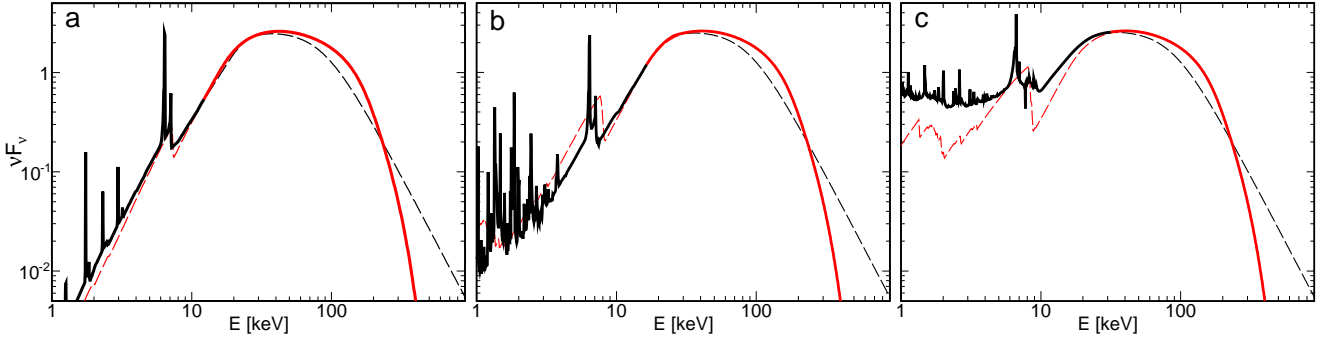


**Figure 4.** Example rest-frame reflection spectra at  $kT_e = 100$  keV. The solid curves, which change the colour from black to red, show the reflection spectra of our model `hreflect` for  $\Gamma = 1.7$ ,  $kT_{bb} = 1$  eV,  $\theta_o = 9^\circ$  and (a)  $\xi = 1$ , (b)  $\xi = 100$  and (c)  $\xi = 1000$ . The black curves (solid at low energies and dashed at high energies) and the red curves (dashed at low energies and solid at high energies) show the reflection spectra of `xillverCp` and `ireflect`, respectively. In all models, the irradiating radiation spectra are normalized at 1 keV.

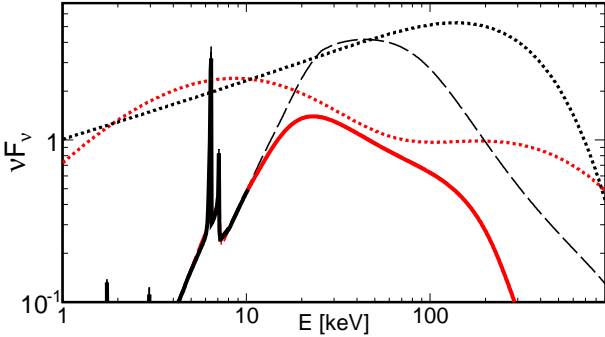


**Figure 5.** Example rest-frame reflection spectrum at a high electron temperature,  $kT_e = 500$  keV. The solid curve, which changes the colour from black to red, shows the reflection spectrum of our model `hreflect` for  $\xi = 1$  and the incident spectrum with  $\Gamma \approx 1.7$  (fitted in the 1–20 keV range and corresponding to  $\tau \approx 0.05$ ),  $kT_{bb} = 50$  eV and  $\theta_o = 30^\circ$ . The red and black dotted curves show the incident spectra of `compps` (used in `hreflect`), and `nthcomp` with  $\Gamma = 1.7$  (used in `xillverCp`), respectively. The dashed curve shows the reflection spectrum of `xillverCp`. We see that at high electron temperatures the `nthcomp` incident spectrum strongly deviates from the actual Comptonization spectrum, and consequently its reflected spectrum strongly deviates from the true one.

gravitational redshift of the direct lamppost emission is taken into account.

Furthermore, `compps` properly describes departures from a power-law at relativistic electron temperatures, with individual scattering orders seen in the Comptonization spectra. In such cases, the spectra in the X-ray range depend on  $T_{bb}$ , as illustrated in Fig. 2. For  $kT_{bb} \gtrsim 10^2$  eV, which is the case of seed photons produced by thermal emission from an accretion disc in a binary, such departures are seen at  $kT_e \gtrsim 300$  keV. For  $kT_{bb} \lesssim 1$  eV, which case approximates Comptonization of seed photons produced by cyclo/synchrotron emission, the X-ray spectrum is formed by mixing of the 2nd and higher scattering orders, which gives a shape closer to a power-law. In Fig. 3, we show an approximate limit on  $kT_e$  for a given  $\Gamma$  for the spherical geometry and two values of  $kT_{bb}$ , above which the Comptonization spectrum deviates significantly from a power-law.

In order to facilitate comparison with other models parametrized by the photon spectral index,  $\Gamma$ , we have also tabulated the  $\Gamma(\tau, T_e)$  relationship at  $kT_{bb} = 1$  eV for a sphere and slab (geometry=0, 1, respectively), where  $\Gamma$  is the photon index fitted

in the 1–20 keV range. Inverting the fitted relationship to  $\tau(\Gamma, T_e)$  allows us to use  $T_e$  and  $\Gamma$  as free parameters in a version of our model. The number intensity of the scattered photons in the local rest-frame is denoted below by  $N_{PS}(E)$ , and the explicit dependence on the model parameters is indicated as either  $N_{PS}(E; T_e, T_{bb}, \tau)$  or  $N_{PS}(E; T_e, \Gamma)$ .

In addition, we have also developed versions of our models for the (phenomenological) e-folded power-law shape of the incident spectrum, which specific intensity is given by

$$N_{EPL} \propto E^{-\Gamma} \exp\left(\frac{-E}{E_{cut}}\right), \quad (1)$$

where  $E_{cut}$  is the e-folding, or cutoff, energy.

### 3 REST-FRAME REFLECTION

The spectrum of the reflected radiation in the disc rest frame used by us at low X-ray energies, namely below  $E_{merge} \approx 10$ –30 keV (with the exact value dependent on the ionization parameter), is given by that of the constant-density model `xillverCp` (García & Kallman 2010 and following work), which assumes the incident spectrum of `nthcomp`. The ionization parameter is defined in a usual way (e.g., García & Kallman 2010),

$$\xi \equiv \frac{4\pi F_{irr}}{n_e}, \quad (2)$$

where  $F_{irr}$  is the irradiating flux in the 13.6 eV–13.6 keV photon energy range, and  $n_e$  is the electron density of the reflecting medium. In the current version,  $n_e = 10^{15} \text{ cm}^{-3}$  (characteristic of inner discs in active galactic nuclei) is assumed, following the value used in `xillverCp`. For a given  $\xi$ ,  $F_{irr} \propto n_e$ , and thus the effective temperature of the reprocessed emission (neglecting any intrinsic dissipation), is  $T_{eff} \propto n_e^{1/4}$ . While the reflected emission is far from a blackbody, the reprocessed part still forms a hump at low energies with  $\langle E \rangle \propto n_e^{1/4}$ , as seen, e.g., in Fig. 4 of García et al. (2016). At low densities,  $n_e \ll 10^{15} \text{ cm}^{-3}$ , the reflector ionization state is independent of  $n_e$ , and the reflected spectra are also only weakly dependent on it, with the main effect being the average energy of the soft, quasi-thermal, hump. However, processes with rates proportional to  $n_e^2$  (e.g., bremsstrahlung heating and cooling, collisional de-excitation, three-body recombination) become important at high densities, and the ionization state is then significantly dependent on  $n_e$ , see García et al. (2016).

For  $n_e = 10^{15} \text{ cm}^{-3}$ , the reflected spectrum of `xillverCp` is the most accurate one available in `xspec`. At  $E \geq E_{\text{merge}}$ , we use the model `ireflect` convolved with `compps`. The convolution model `ireflect` (Magdziarz & Zdziarski 1995) gives an exact reflection for any shape of primary radiation for given reflector opacities. However, its built-in treatment of ionization is rather approximate for any value of  $\xi$  (of Done et al. 1992), and it fails at high values of  $\xi$ . However, at  $E \geq E_{\text{merge}}$ , there are virtually no lines or edges in the reflected spectrum, and that shortcoming is of no importance. Our hybrid model of rest-frame reflection is called `hreflect`.

Fig. 4 illustrates the merging of the reflection spectra of `ireflect` and `xillverCp` for a  $kT_e$  below the limit shown in Fig. 3, where the low energy part of the `compps` spectrum has a power-law shape and unambiguously determines the  $\Gamma$  parameter of `xillverCp`, and for the inclination angle of the observer of  $\theta_o = 9^\circ$ . We note, however, that `xillverCp` uses the incident spectrum of `nthcomp`, which dependence on  $kT_e$  for  $kT_e \gtrsim 100 \text{ keV}$  does not precisely correspond to the actual high-energy extent of the `compps` spectrum. Models using the incident e-folded power law can also be used to assess the resulting inaccuracies.

At temperatures above the limit shown in Fig. 3, the high-energy part of our rest-frame reflection (i.e., that computed with `ireflect`) is still exact. In order to find the low energy part of reflection, we fit  $N_{\text{PS}}(E)$  with a power-law in the 1–20 keV range and use the fitted  $\Gamma$  as the `xillverCp` parameter, as illustrated in Fig. 5. We see that now the actual incident and reflected spectra are very different from those calculated with `xillverCp`. This is a major shortcoming of `xillverCp`, especially important for cases of the primary source located close to the BH horizon, in which case the primary radiation is blueshifted by a large factor with respect to the observed emission.

We note that in computing the rest-frame reflection, we lose the information about the actual angular distribution of the irradiating photons in the disc frame. This is because `xillverCp` assumes a fixed incidence angle of  $45^\circ$ , while `ireflect` convolves the primary spectrum with Green functions averaged over the incidence angle for an isotropic source above a slab.

In the case of the incident e-folded power-law spectrum, equation (1), the reflection at high energies (given by `ireflect`) is the same as that of the `pexriv` model (Magdziarz & Zdziarski 1995). We then merge it with the `xillver` model, which also uses the e-folded power-law incident spectrum. These models can also be used to check if the shape of the cutoff significantly affects the soft X-ray part of reflection.

## 4 RELATIVISTIC MODIFICATIONS TO THE INCIDENT SPECTRUM AND REFLECTION

We have then developed models taking into account the relativistic effects on emission from a given point in the Kerr metric. We take into account those effects acting on the primary spectrum and on the reflection. We allow the disc to extend to an arbitrary radius above the horizon. We assume the disc to have no intrinsic dissipation, similarly to most of previous works on the subject (but with the exception of, e.g., Ross & Fabian 2007).

### 4.1 The lamppost

In the lamppost geometry, two identical, point-like X-ray sources are symmetrically located on the BH rotation axis perpendicular to

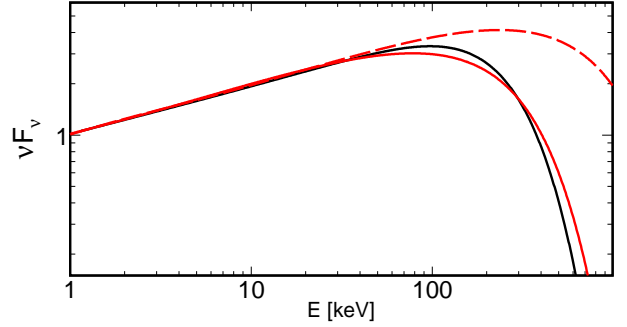


**Figure 6.** The effect of the gravitational redshift on thermal Comptonization spectra. The solid black and dashed red curves show the rest-frame spectra of our model,  $E^2 N_{\text{PS}}$ , for  $kT_e = 100$  and  $300 \text{ keV}$ , respectively,  $\Gamma = 1.7$  and  $kT_{\text{bb}} = 1 \text{ eV}$ . The solid red curve shows the spectrum for  $kT_e = 300 \text{ keV}$  redshifted by  $g_{\text{so}} = 1/3$ . We see it significantly differs from the spectrum calculated for  $g_{\text{so}} kT_e$ .

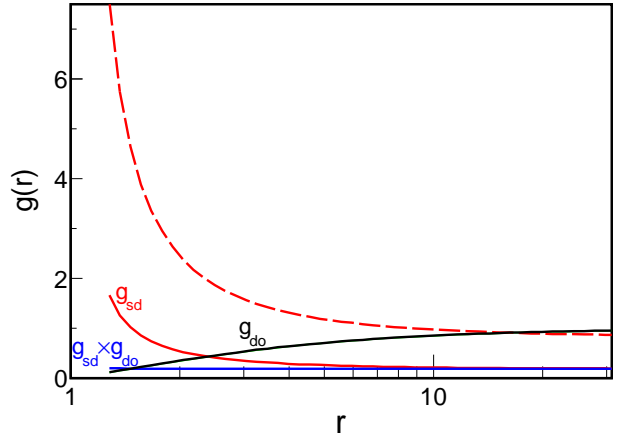


**Figure 7.** Example energy-shift factors. The red, black and blue solid curves show the lamp-to-disc,  $g_{\text{sd}}$ , and disc-to-observer,  $g_{\text{do}}$ , factors and their product, respectively, for  $h = 1.3$  and  $a = 0.998$ . The  $g_{\text{do}}$  factor is at  $\theta_o = 9^\circ$  and weighted by the number of observed photons. The dashed red curve shows the lamp-to-disc energy-shift factor,  $g_{\text{sd}}$ , for  $h = 6$ . We see the energy-shift factors can be both  $< 1$  and  $> 1$ .

a surrounding flat disc. A further assumption adopted in all previous works is that the lamppost is not rotating, and we follow it as well. Our `xspec` model for the observed spectra of thermal Comptonization and its reflection is called `reflkerr_lp`. Usually, we consider the disc to be truncated at an inner radius  $r_{\text{in}} \geq r_{\text{ISCO}}(a)$ , where ISCO is the innermost stable circular orbit and  $a$  is the BH dimensionless angular momentum. However, the free-falling medium below the ISCO can be still optically thick at high accretion rates (Reynolds & Begelman 1997), and therefore we allow  $r_{\text{in}} > r_{\text{hor}}(a)$ , where  $r_{\text{hor}}$  is the horizon radius. The height of the source,  $h$ , and the radial distance in the disc plane,  $r$ , are in units of the gravitational radius,  $R_g = GM/c^2$ , where  $M$  is the BH mass. Our model uses the rest-frame spectra of the primary and reflected radiation calculated with `hreflect`, and convolves them with the Kerr metric transfer functions to compute the spectra of radiation received by a distant observer as well as that irradiating the disc surface.

In Niedźwiecki & Zdziarski (2018), we investigated effects related to optical thinness of the region below  $r_{\text{in}}$  in models with a truncated disc. We found that the bottom lamp may contribute sig-

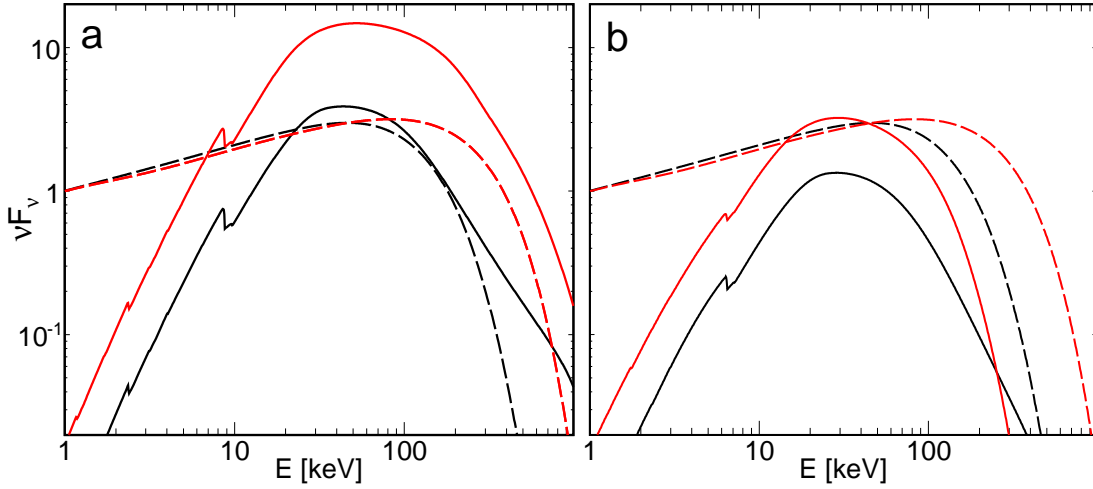


**Figure 8.** A comparison of observed lamppost spectra predicted by the `reflkerr_lp` (red) and `relxilllpCp` v. 1.0.4 (black) models at a low  $h = 2$ . The reflection and direct components are shown by the solid and dashed curves, respectively. The other parameters are: (a)  $\theta_0 = 75^\circ$ , (b)  $9^\circ$ , and  $a = 0.998$ ,  $r_{\text{in}} = r_{\text{ISCO}} \approx 1.24$ ,  $r_{\text{out}} = 1000$ ,  $\Gamma = 1.7$ ,  $kT_e = 200$  keV,  $\xi = 1$ . Both models use the actual lamppost reflection fraction, i.e., `fixReflFrac = 1` is set in `relxilllpCp`. The strong reflection component in (a) is due to light bending of the photons emitted by the lamp, which causes many more emitted photons to hit the disc than go to the observer. Since the reflected photons are preferentially emitted at large angles with respect to the axis, due to both the Kerr metric effects and Doppler boosting, the observed reflection strength is much higher in (a) than in (b).

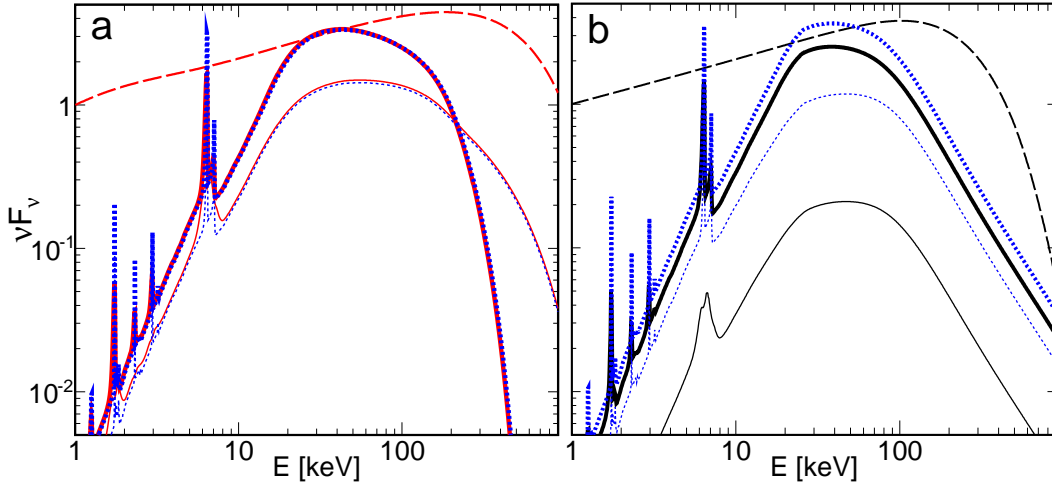


**Figure 9.** A comparison of observed lamppost spectra predicted by (a) the `reflkerr_lp` and (b) `relxilllpCp` models at a high  $h = 100$ . The GR reflection, static reflection and direct components are shown by the solid, blue dotted and dashed curves, respectively. The thick and thin lines give the reflection spectra for  $\theta_0 = 9^\circ$  and  $75^\circ$ , respectively. The other parameters are the same as in Fig. 8. The static reflection spectra use `hreflect` in (a) and `xillverCp` in (b). Given the large height of the primary source, the GR effects should be very small, and the static and GR-corrected reflection spectra should be almost identical, which they are in the panel (a). However, they strongly differ in the panel (b).

nificantly both to the directly observed and to the reflected radiation when  $r_{\text{in}} \gtrsim 3$ . In the general version of our model, we take into account these effects, as well as a secondary effect related with radiation of the top lamp crossing twice the equatorial plane at  $r < r_{\text{in}}$  (see fig. 4b in Niedźwiecki & Zdziarski 2018). However, we consider also a simpler version, referred to below as a ‘simple LP model’, neglecting these effects, i.e. taking into account only radiation of the top lamp which does not cross the equatorial plane. The user can choose this version by setting a parameter to compare our model with other computations, e.g. of `relxilllpCp`, or to estimate the contribution of the additional effects included in our model.

The flux of the primary radiation seen at infinity is computed

by means of a photon transfer function,  $\mathcal{T}_{\text{so}}$ , which describes travel of photons from the lamps to the distant observer. It takes into account the reduction of the observed flux due to light bending, photon trapping and time dilation. We consider separately the transfer of radiation from the top lamp which does not cross the equatorial plane, described by  $\mathcal{T}_{\text{so},1}(a, h)$ , and radiation from the bottom lamp plus radiation from the top lamp deflected by the BH (Niedźwiecki & Zdziarski 2018), described by  $\mathcal{T}_{\text{so},2}(a, h, r_{\text{in}}, \theta_0)$ . In general, we consider both components, in which case the observed photon flux is

$$N_{\text{direct}}(E_o, \theta_o) = \frac{1}{D^2} (\mathcal{T}_{\text{so},1} + \mathcal{T}_{\text{so},2}) N_{\text{PS}}(E_o/g_{\text{so}}), \quad (3)$$

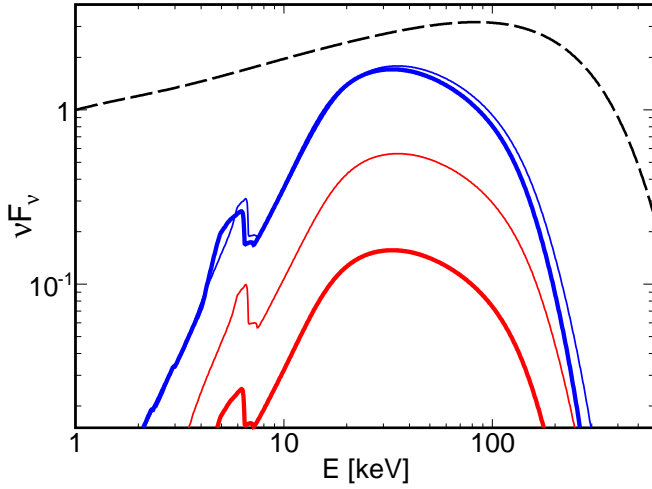


**Figure 10.** An example illustration of the effect of the emission of the bottom lamp and of the emission of the top lamp circling around the BH (i.e., crossing twice the equatorial plane). The solid curves show the observed reflection spectra for  $h = 2$ ,  $a = 0.998$ ,  $r_{\text{in}} = 4.9$ ,  $r_{\text{out}} = 1000$ ,  $\Gamma = 1.7$ ,  $kT_e = 200$  keV,  $\xi = 1$ ,  $kT_{\text{bb}} = 50$  eV,  $\theta_o = 9^\circ$  (thick lines) and  $30^\circ$  (thin lines), computed with `reflkerr_lp` for the simple LP case (blue) and the general model (red). The black dashed curve shows the observed primary spectrum. We see the accurate reflected spectra are much weaker with respect to the observed primary emission than those in the approximate (simple LP) case. In the shown case, this is due mostly to the primary emission of the bottom lamp gravitationally focused toward the observer, which enhances the observed primary flux by as much as a factor of 10 in the case of  $\theta_o = 9^\circ$ . Since our plotted primary spectra are normalized to unity at 1 keV, this enhancement is seen here as a decrease of the amplitude of the reflection.

where  $D$  is the distance to the source,  $g_{\text{so}} = E_o/E_s [= 1/(1+z)]$ , where  $z$  is the redshift] is the photon energy-shift factor, and the subscripts 's' and 'o' denote quantities measured in the local source frame and those observed at infinity, respectively. In the simple LP case, we compute the observed flux taking into account only  $\mathcal{T}_{\text{so},1}$ , in which case the observed photon flux is

$$N_{\text{direct}}(E_o) = \frac{1}{D^2} \mathcal{T}_{\text{so},1} N_{\text{PS}}(E_o/g_{\text{so}}). \quad (4)$$

Our treatment of the directly observed radiation is exact, i.e., we use the actual rest-frame spectrum redshifted by  $g_{\text{so}}$ . We note that the shape of the high energy cutoff in the redshifted spectrum differs from the shape of the spectrum computed for temperature scaled by the same  $g_{\text{so}}$  factor, i.e.,  $N_{\text{PS}}(E_o; g_{\text{so}} T_e, \Gamma)$  differs from  $N_{\text{PS}}(E_o/g_{\text{so}}; T_e, \Gamma)$ , as illustrated in Fig. 6.

The spectrum of radiation irradiating the disc is given by the `compps` spectrum shifted by  $g_{\text{sd}}$ ,  $N_{\text{PS}}(E_d/g_{\text{sd}})$ , where  $g_{\text{sd}} = E_d/E_s$  is the radius-dependent energy-shift factor and the subscript 'd' denotes quantities measured in the local frame co-moving with the disc. For the transfer of photons from the lamps to the disc, we again consider separately direct illumination by the top lamp, described by  $\mathcal{T}_{\text{sd},1}(a, r, h)$ , and illumination by the bottom lamp, described by  $\mathcal{T}_{\text{sd},2}(a, r, h, r_{\text{in}})$ . Illumination by the top lamp radiation deflected by the BH and crossing twice the equatorial plane is always negligible. The photon flux irradiating the disc at distance  $r$  is

$$N_d(E_d, r) = \mathcal{T}_{\text{sd}}(a, r, h) N_{\text{PS}}(E_d/g_{\text{sd}}), \quad (5)$$

where  $\mathcal{T}_{\text{sd}} = \mathcal{T}_{\text{sd},1} + \mathcal{T}_{\text{sd},2}$  in the general case and  $\mathcal{T}_{\text{sd}} = \mathcal{T}_{\text{sd},1}$  in the

simple LP case. The spectrum of reflected radiation from a unit area of the disc at distance  $r$  seen at infinity is

$$N_o(E_o, \theta_o, r) = \frac{1}{D^2} \int \mathcal{T}_{\text{do}}(a, r, \theta_d, \theta_o, g_{\text{do}}) N_{\text{ref}}(E_o/g_{\text{do}}, r, \theta_d) d\mu_d dg_{\text{do}}, \quad (6)$$

where  $\mu_d = \cos \theta_d$ ,  $\theta_d$  is the emission angle in the disc frame,  $g_{\text{do}} = E_o/E_d$  and  $N_{\text{ref}}$  is the photon number intensity of the reflected radiation in the disc frame, corresponding to the irradiating flux given by equation (5). The transfer functions  $\mathcal{T}_{\text{sd}}$ ,  $\mathcal{T}_{\text{do}}$  and the energy-shift factors  $g_{\text{sd}}$ ,  $g_{\text{do}}$  treat the special and general relativistic effects (GR) affecting both the irradiating and observed fluxes. The total observed photon flux of the reflected radiation is

$$N_{\text{reflected}}(E_o, \theta_o) = \int_{r_{\text{in}}}^{r_{\text{out}}} N_o(E_o, \theta_o, r) 2\pi r dr. \quad (7)$$

Our tabulated transfer functions allow us to compute the observed disc reflection up to  $r_{\text{out}} = 1000$ .

Fig. 7 shows example values of energy-shift factors affecting the irradiating and observed disc radiation. We note that for low  $\theta_o$ , the effective redshift, i.e.  $g_{\text{sd}}g_{\text{do}}$ , approximately equals that affecting the direct radiation, i.e.  $g_{\text{so}}$ , e.g.,  $\approx 0.18$  for  $h = 1.3$ . In models with large values of  $h$ , the radiation illuminating the disc close to ISCO is strongly blueshifted, e.g.  $g_{\text{sd}} \gtrsim 4$  at  $r < 1.5$  for  $h > 6$ , as shown by the dashed curve. This effect is typically not important for the observed reflected radiation, as for large  $h$  the contribution of radiation reflected from this inner edge of the disc is small.

Except for the approximations noted above in computing the rest-frame reflection, `reflkerr_lp` involves the exact implementation of the model of Niedźwiecki & Życki (2008). However, it does not include the second-order reflection, as the spectrum of radiation returning to the disc strongly deviates from a power-law and therefore `xillverCp` cannot be applied to compute the reflection in the disc frame. This is an important shortcoming of this model for some cases, see fig. 4 of Niedźwiecki et al. (2016).

The transfer functions are tabulated in a grid including 12 values of  $a$ , spaced uniformly at  $a \leq 0.9$  (0.9, 0.8, ...) and more densely at  $a > 0.9$  (0.95, 0.98, 0.998), and 50 logarithmically spaced values of  $h$  up to  $h = 100$ . The calculated trajectories were tabulated in 10 uniform bins of  $\mu_d$  (which corresponds to the angular accuracy of both `ireflect` and `xillverCp`), 100 uniform bins of  $\cos \theta_o$ , 100 logarithmic bins of  $r$  and 2000 uniform bins in  $g$ . The total number of calculated trajectories was  $10^8$  for each pair of  $a$  and  $h$  in computing  $\mathcal{T}_{\text{so}}$  and  $\mathcal{T}_{\text{sd}}$ , and  $10^8$  for each pair of  $a$  and  $r$  in computing  $\mathcal{T}_{\text{do}}$ .

Figs. 8 and 9 compare the spectra predicted by `reflkerr_lp` and the current version, 1.0.4, of `relxilllpCp` for an untruncated disc. At  $h = 2$  (Fig. 8), many more directly emitted photons hit the disc than go to the observer due to light bending. Also, the reflected photons are preferentially emitted at large angles with respect to the axis, due to both the Kerr metric effects and Doppler boosting. Therefore the observed reflection strength is much higher for  $\theta_o = 75^\circ$  than for  $\theta_o = 9^\circ$ . In addition, the redshift of the direct radiation at  $\theta_o = 75^\circ$  is about twice as strong as the effective redshift of the reflected emission. This causes a relative shift of the two spectra, and, e.g., the observed reflected flux at 1 MeV is a few tens times higher than the observed direct flux.

We note a good agreement between the spectral shapes of the low energy parts (at  $E \lesssim 30$  keV) of the reflected components. However, we note systematic differences by a factor of  $\sim 2-5$  between the observed reflection strengths predicted by `reflkerr_lp` and `relxilllpCp` (for `fixRefIFrac` = 1, giving the actual lamp post

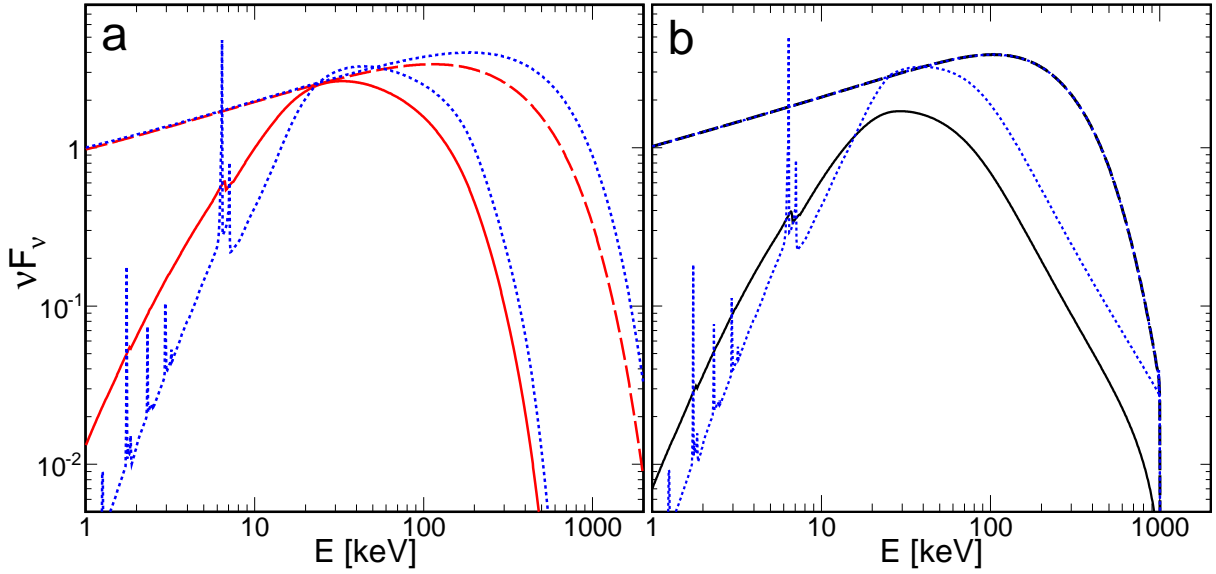


**Figure 11.** Comparison of results for coronal reflection using (a) `reflkerr` and (b) `xillverCp` (b). (a): The red dashed and solid curves show the observed primary and reflection spectra, respectively, computed with `reflkerr` for  $a = 0.998$ ,  $r_{\text{in}} = r_{\text{ISCO}} \approx 1.24$ ,  $r_{\text{out}} = 1000$ ,  $\theta_o = 30^\circ$ ,  $\Gamma = 1.7$ ,  $kT_e = 200$  keV,  $\xi = 1$ ,  $q_1 = 5$ ,  $q_2 = 3$  and  $r_{\text{br}} = 5$ . (b): The black dashed and solid curves show the observed primary and reflection spectra, respectively, computed with `relxillCp` for the same model parameters as in (a). The blue dotted curves on both panels show the corresponding rest-frame spectra, `compps` and `hreflect` on (a) and `nthcomp` and `xillverCp` on (b).

reflection fraction), even at a large  $h = 100$ , where the GR effects are negligible and the kinematic collimation due to disc rotation is a minor (a few per cent) effect, so the reflection strength should agree with the nonrelativistic models.

At  $E \gtrsim 30$  keV, there are also differences in the spectral shape related with a more accurate treatment of both the reflected and primary component in `reflkerr_lp` (Sections 2 and 3). For electron temperatures above the limit shown in Fig. 3, the spectral shapes of the reflected components of `reflkerr_lp` and `relxillCp` will differ at all energies.

In the case of the e-folded power-law incident spectrum,  $N_{\text{PS}}$  in equations (3–5) is to be replaced by  $N_{\text{EPL}}$ . The directly observed cut-off energy equals  $g_{\text{so}} E_{\text{cut}}$  and the radius-dependent cut-off of the incident spectrum is  $g_{\text{sd}} E_{\text{cut}}$ .

The `reflkerr_lp` model takes into account the emission of the bottom lamp, neglected in `relxillCp`, which will strongly affect the reflection strength in models with  $r_{\text{in}} \gtrsim 3$ . Fig. 10 illustrates the importance of this effect. In the shown examples, the primary emission is strongly enhanced when the (gravitationally focused) emission of the bottom lamp is included, while the reflected emission remains almost the same. However, since we plot the incident spectra normalized to unity at 1 keV, this is seen as a decrease of the reflection amplitude.

We emphasize that properly assessed reflection amplitude gives an important constraint on the lampost model, where both the fraction and the radial distribution of photons illuminating the disc surface are fully determined by the height of the primary X-ray source. Then, the radial emission profile is strictly related to assumed geometry, and treating the fraction of reflected photons as a free parameter leads to results which are not self-consistent. Still, our model allows the user to make it free.

## 4.2 Relativistic reflection from a corona above a disc

Our second model, `reflkerr`, approximates the geometry of a corona covering the accretion disc at a low scale-height, and co-rotating with it. Following previous works, we approximate it by a broken-power law emissivity profile of the corona. As in the lampost model, no intrinsic dissipation in the disc is taken into account. The locally produced radiation is calculated using `compps` for the slab geometry, assuming it to have the rest-frame spectrum constant with radius.

The observed spectrum from a unit area is given by

$$N_o(E_o, \theta_o, r) = \frac{1}{D^2} \int \mathcal{T}_{\text{do}}(a, r, \theta_d, \theta_o, g_{\text{do}}) N_{\text{em}}(E_o/g_{\text{do}}, \theta_d) \epsilon(r) d\mu_d dg_{\text{do}}, \quad (8)$$

$$N_{\text{em}}(E_d, \theta_d) = N_{\text{PS}}(E_d, \theta_d) + RN_{\text{ref}}(E_d, \theta_d), \quad (9)$$

$$\epsilon(r) = \begin{cases} (r/r_{\text{br}})^{-q_1}, & r \leq r_{\text{br}}; \\ (r/r_{\text{br}})^{-q_2}, & r \geq r_{\text{br}}, \end{cases} \quad (10)$$

where the normalization of  $N_{\text{PS}}$  is at  $r_{\text{br}}$ .  $q_1$  and  $q_2$  are the parameters of the broken power-law emissivity, and  $R$  is the reflection fraction, defined in the same way as that in the codes `compps` and `ireflect`, i.e.,  $R = 1$  corresponds to a local reflection of an isotropic point source from a semi-infinite slab, neglecting at this point any attenuation of the reflected component due to scattering in the corona. Equation (8) is similar to equation (6), but now the locally emitted spectrum includes both the primary and reflected components. Note that in the slab geometry, the Comptonization photon intensity,  $N_{\text{PS}}$  depends on the local emission angle,  $\theta_d$ . The total observed photon flux is

$$N_{\text{obs}}(E_o, \theta_o) = \int_{r_{\text{in}}}^{r_{\text{out}}} N_o(E_o, \theta_o, r) 2\pi r dr. \quad (11)$$

We have also developed a version of the coronal model for the incident spectrum of the form of an e-folded power law, in which case  $N_{\text{PS}}$  in equation (9) is replaced by  $N_{\text{EPL}}$ .

**Table 1.** The best-fit parameters of the model with two lamppost components above an untruncated disc for NGC 4151. Model 1:  $\text{TBabs}*(\text{NA1}*\text{NA2}*\text{gabs}*\text{WA}*(\text{nthcomp}+\text{relxilllpCp}+\text{relxilllpCp}+\text{zgauss}+\text{zgauss})+\text{nthcomp})$ . Model 2:  $\text{TBabs}*(\text{NA1}*\text{NA2}*\text{gabs}*\text{WA}*(\text{reflkerr\_lp}+\text{reflkerr\_lp}+\text{zgauss}+\text{zgauss})+\text{nthcomp})$ . The Galactic absorbing column (TBabs), is set to  $N_{\text{H}} = 2.3 \times 10^{20} \text{ cm}^{-2}$  in both models. The reflection fractions are free in the model 1, and they are kept at the physical values in the model 2. The second, unabsorbed (except for the Galactic ISM)  $\text{nthcomp}$  component has the spectral index linked to  $\Gamma$  of the fitted LP components. Parameters denoted with '(f)' were fixed in the fitting. Since our fits are intended to illustrate the difference in the different modelling, we do not show the confidence regions of the fitted values.

Model component	Model 1	Model 2
<b>neutral absorber 1 (NA1):</b>	partcov*ztBabs	
$N_{\text{H}} [10^{22} \text{ cm}^{-2}]$	8.8	9.0
covering fraction	1.0	1.0
<b>neutral absorber 2 (NA2):</b>	partcov*ztBabs	
$N_{\text{H}} [10^{22} \text{ cm}^{-2}]$	21.9	19.7
covering fraction	0.45	0.46
<b>warm absorber (WA):</b>	warmabs	
$N_{\text{H}} [10^{22} \text{ cm}^{-2}]$	1.2	1.9
$\log_{10}(\xi) [\text{erg cm s}^{-1}]$	2.85	3.01
$v_{\text{turbulent}} [\text{km s}^{-1}]$	3000	
<b>thermal Comptonization:</b>	nthcomp	
normalization	0.045	-
$\Gamma$	1.71	-
$kT_{\text{e}} [\text{keV}]$	400 (f)	-
$kT_{\text{bb}} [\text{keV}]$	0.05	-
<b>lamppost components</b>	relxilllpCp	reflkerr_lp
$a$	0.998 (f)	
$\theta_0 [^\circ]$	3	19.8
$r_{\text{in}} [r_{\text{g}}]$	$r_{\text{ISCO}}$ (f)	
$r_{\text{out}} [r_{\text{g}}]$	1000 (f)	
$\log_{10}(\xi) [\text{erg cm s}^{-1}]$	3.0	3.0
$Z_{\text{Fe}}$	2.5	2.5
<b>LP<sub>1</sub></b>		
normalization	205	0.025
$h [r_{\text{g}}]$	1.17 (f)	
$\Gamma$	1.71	1.71
$kT_{\text{e}} [\text{keV}]$	400 (f)	
<b>LP<sub>2</sub></b>		
norm	$7.3 \times 10^{-4}$	0.013
$h [r_{\text{g}}]$	15 (f)	
$\Gamma$	1.71	1.71
$kT_{\text{e}} [\text{keV}]$	400 (f)	
$\chi^2/\text{DoF}$	848/684	1238/681

We note that our model takes into account the gravitational redshift of the X-ray radiation produced in the corona, which effect has been neglected in `relxill` (including the current v. 1.0.4). The corona co-rotates with the disc, so its radiation is also affected by the same kinematic effects as the reflected radiation. Fig. 11 shows example coronal spectra calculated with `reflkerr` and `relxill`. We see substantial differences, including that in the amplitude of the reflected component.

## 5 APPLICATION TO NGC 4151

We then present an example of our lamppost model results for the simultaneous *Suzaku* and *NuSTAR* observation of the Seyfert galaxy NGC 4151 on 2012 November 11–14. We compare our model with the lamppost model previously applied to these data (`relxilllpCp`), which allows us to illustrate the importance of the proper modelling of gravitational redshift. We use the same data as Keck et al. (2015) and Beuchert et al. (2017), and apply the same data reduction procedure. For the spectral analysis, we use the data in the range of 2.5–9 keV from the XIS front-illuminated (XIS 0 + XIS 3) detectors, 2.5–7.5 from the XIS back-illuminated (XIS 1) detector, 14–60 keV from the PIN, all on board *Suzaku*, and 5–79 keV from the *NuSTAR* FPM A and B detectors.

Keck et al. (2015) and Beuchert et al. (2017) previously analysed these data with lamppost models. They claimed the presence of an untruncated accretion disc around a rapidly rotating BH, illuminated by two sources, one of them located very close to the BH horizon. Here, we assume the parameters of the model fitted in Beuchert et al. (2017), including two lamppost components at  $h_1 = 1.17$  and  $h_2 = 15$ , the disc truncated at  $r_{\text{in}} = r_{\text{ISCO}}$ , and  $a = 0.998$ . Our aim here is to illustrate the GR effects by comparing two models with the same lamppost parameters, therefore in all cases below we fixed these values.

We consider two models. In the model 1, we follow Beuchert et al. (2017), i.e., we include two lamppost reflection components, LP<sub>1</sub> and LP<sub>2</sub>, described by `relxilllpCp` and one thermal Comptonization component described by an independent `nthcomp` spectrum, and we allow for free normalizations of these three spectral components. This model neglects the GR redshift of the primary emission as well as it does not use the physical reflection fractions. In the model 2, we use two `reflkerr_lp` components including both the primary and reflected radiation and in both we fix the physical reflection fraction. In both models, we also fix  $kT_{\text{e}} = 400$  keV (following Beuchert et al. 2017) and in the model 2 we use a constant  $kT_{\text{bb}} = 1$  eV, which allows us not to include slight deviations from a power law which would be present for  $kT_{\text{bb}} \sim 10$  eV (which is the characteristic disc temperature at the BH mass and the luminosity of NGC 4151, see, e.g., Lubiński et al. 2010), as can be inferred from Fig. 2. In both models, we also use the same additional spectral components as Beuchert et al. (2017), i.e., a warm absorber, two neutral, partially-covering absorbers, narrow Fe K $\alpha$  and K $\beta$  lines and an additional Comptonization component attenuated only by the Galactic absorption, modelled with `nthcomp` with the same shape as the main Comptonization spectrum.

Our fitting results are shown in Table 1 and Fig. 12. The model 1 gives a good fit, similar to that found in Beuchert et al. (2017). The model 2 gives a significantly worse fit, with  $\Delta\chi^2 \approx 400$ , and a strong residual pattern seen in Fig. 12(b). The discrepancy is related with the redshift of the primary component from  $h_1$ , taken into account in `reflkerr_lp` and neglected in the model 1. Allowing  $kT_{\text{e}}$  to vary in the model 2 does not improve the fit and the fitted value remains  $\approx 400$  keV. Note that  $\Gamma \approx 1.7$  and  $kT_{\text{e}} \approx 400$  keV are close to the limit shown in Fig. 3, and then an increase of  $T_{\text{e}}$ , which could compensate for the redshift, would also lead to departures from a power-law shape and a disagreement with the data.

The compactness parameter for the source at  $h = 1.17$  in the model 2 is  $\ell \approx 5 \times 10^6$  (for photons with rest-frame energies larger than 2 keV), which, at the rest-frame  $kT_{\text{e}} = 400$  keV, yields the pair production rate larger by many orders of magnitude than the annihilation rate (Niedźwiecki et al. 2016).

We note that the physical reflection fractions used in the model



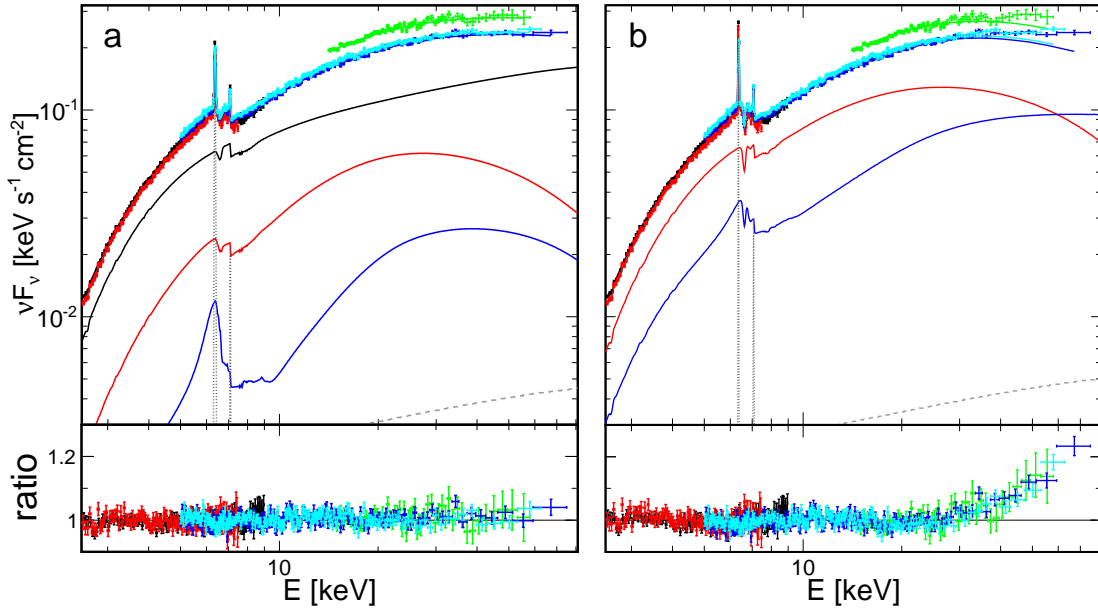


**Figure 12.** The fits to the X-ray spectrum of NGC 4151. The upper panels show the unfolded data and the model spectral components. The lower panels show the data-to-model ratios. The colours in the data indicate the XIS 0+3 (black), XIS 1 (red), PIN (green), FPM A (blue) and FPM B (cyan). (a) The model 1, following [Beuchert et al. \(2017\)](#). The black, red and blue curves show the primary component (nthcomp) and two reflection components (relxilllpCp) of the lamps at  $h_1 = 1.17$  and  $h_2 = 15$ , respectively. The reflection fractions were free in the fit. (b) The model 2, with the lamppost components modelled with reflkerr\_lp. The physical reflection fraction was fixed for both components. The red and blue curves show the total (primary+reflection) spectra of the LP components at  $h_1 = 1.17$  and  $h_2 = 15$ , respectively. The gray lines in (a) and (b) show the narrow Fe  $K\alpha$  and  $K\beta$  lines and the additional unabsorbed Comptonization component. All the model components are normalized to the XIS0+3 data.

2 are crucial for the above discrepancy. If we use our model with free reflection fractions (which is unphysical), we find we can obtain a good fit. It includes a weakly redshifted primary spectrum of  $LP_2$  stronger than that of  $LP_1$ , and completely dominating at high energies.

## 6 SUMMARY

We have presented the computational framework of our new relativistic reflection models, `reflkerr_lp` and `reflkerr`<sup>1</sup>, for two geometries, the lamppost and the disc corona, respectively. In both cases, we assume that the primary X-ray radiation is produced by thermal Comptonization and we compute it using the iterative code of [Poutanen & Svensson \(1996\)](#), which is one of the most accurate publicly available models of this process. It allows us to correctly describe spectra produced at relativistic electron temperatures, which is particularly important for the lamppost geometry, where such temperatures are required for a low height above the horizon of the irradiating source. This Comptonization model also allows us to study the dependence on the seed photons energy as well as on the source geometry. We have chosen a sphere as an appropriate case for the lamppost and a slab for the disc corona. In addition, we have developed versions of the models for the phenomenological incident spectrum given by an e-folded power law.

We use a hybrid model of the rest-frame reflection from a photoionized medium, which combines the model of [García & Kallman \(2010\)](#) in the soft X-ray range with the exact model for Compton reflection of [Magdziarz & Zdziarski \(1995\)](#) in

the hard X-ray and soft  $\gamma$ -ray range. This probably gives the most accurate treatment of ionized reflection using currently available models.

We apply the photon transfer functions in the Kerr metric to compute the directly observed and reflected photon flux and, for the lamppost geometry, the flux irradiating the disc. The transfer functions for the lamppost geometry include photons crossing the equatorial plane within the truncation radius, which allows us to take into account the full contributions of primary sources located on both sides of the accretion disc to the directly observed and to the reflected radiation.

We have compared our `reflkerr` and `reflkerr_lp` models with the previous reflection models of `relxill` and `relxilllp` and found an overall agreement of their spectral shapes in the soft X-ray range, which shows that computation of the transfer of disc radiation gives consistent results in both families of models. However, we note significant differences between the predicted reflection strengths, which in turn indicate some inconsistencies in computations of the transfer of the primary radiation to the disc and/or to the observer. These differences occur even at very large heights in the lamppost models, where an accuracy test can be made by comparison with the static reflection models. Also, above  $\sim 30$  keV, the spectral shapes of `reflkerr` or `reflkerr_lp` differ from those of `relxill` or `relxilllp` due to a more accurate treatment of both the reflected and primary component in the former.

Application of our `reflkerr_lp` model to X-ray data for NGC 4151 demonstrated the importance of a proper modelling of gravitational redshift acting on the direct radiation from a source close to the horizon, i.e., at the location needed to explain the apparently very broadened reflection components. This redshift cannot be compensated by an increase of electron temperature, even in the data extending only up to  $\approx 80$  keV.

<sup>1</sup> The models can be downloaded at [users.camk.edu.pl/mitsza/reflkerr](http://users.camk.edu.pl/mitsza/reflkerr)

**ACKNOWLEDGEMENTS**

We thank Thomas Dauser and Javier García for discussions, and Tobias Beuchert for a clarification regarding his model. This research has been supported in part by the Polish National Science Centre grants 2013/10/M/ST9/00729, 2015/18/A/ST9/00746 and 2016/21/B/ST9/02388.

**REFERENCES**

- Arnaud K. A., 1996, in Jacoby G. H., Barnes J., eds., *Astronomical Data Analysis Software and Systems V*, ASP Conf. Series Vol. 101, San Francisco, p. 17
- Ballantyne D. R., et al., 2014, *ApJ*, 794, 62
- Baloković M., et al., 2015, *ApJ*, 800, 62
- Basak R., Zdziarski A. A., 2016, *MNRAS*, 458, 2199
- Basak R., Zdziarski A. A., Parker M., Islam N., 2017, *MNRAS*, 472, 4220
- Basko M. M., Sunyaev R. A., Titarchuk L. G., 1974, *A&A*, 31, 249
- Beuchert T., et al., 2017, *A&A*, 603, A50
- Brenneman L. W., et al., 2014, *ApJ*, 788, 61
- Burke M. J., Gilfanov M., Sunyaev R., 2017, *MNRAS*, 466, 194
- Dauser T., Wilms J., Reynolds C. S., Brenneman L. W., 2010, *MNRAS*, 409, 1534
- Dauser T., García J., Wilms J., Böck M., Brenneman L. W., Falanga M., Fukumura K., Reynolds C. S., 2013, *MNRAS*, 430, 1694
- Dauser T., García J., Walton, D. J., Eikmann W., Kallman T., McClintock J., Wilms J., 2016, *A&A*, 590, A76
- Degenaar N., Miller J. M., Chakrabarty D., Harrison F. A., Kara E., Fabian A. C., 2015, *MNRAS*, 451, L85
- Done C., Gierliński M., Kubota A., 2007, *A&ARv*, 15, 1
- Done C., Mulchaey J. S., Mushotzky R. F., Arnaud K. A., 1992, *ApJ*, 395, 275
- Dovčiak M., Karas V., Yaqoob T., 2004, *ApJS*, 153, 205
- Dovčiak M., Muleri F., Goosmann R. W., Karas V., Matt G., 2011, *ApJ*, 731, 75
- Fabian A. C., Rees M. J., Stella L., White N. E., 1989, *MNRAS*, 238, 729
- Fabian A. C., Lohfink A., Kara E., Parker M. L., Vasudevan R., Reynolds C. S., 2015, *MNRAS*, 451, 4375
- Fürst F., et al., 2015, *ApJ*, 808, 122
- García J., Kallman T. R., 2010, *ApJ*, 718, 695
- García J. et al., 2014, *ApJ*, 782, 76
- García J. et al., 2016, *MNRAS*, 462, 751
- Gondek D., Zdziarski A. A., Johnson W. N., George I. M., McNaron-Brown K., Magdziarz P., Smith D., Gruber D. E., 1996, *MNRAS*, 282, 646
- Keck M. L., et al., 2015, *ApJ*, 806, 149
- Lightman A. P., White T. R., 1988, *ApJ*, 335, 57
- Lubiński P., Zdziarski A. A., Walter R., Paltani S., Beckmann V., Soldi S., Ferrigno C., Courvoisier T. J.-L., 2010, *MNRAS*, 408, 1851
- Lubiński P., et al., 2016, *MNRAS*, 458, 2454
- Madejski G. M., et al., 1995, *ApJ*, 438, 672
- Magdziarz P., Zdziarski A. A., 1995, *MNRAS*, 273, 837
- Malizia A., et al., 2008, *MNRAS*, 389, 1360
- Marinucci A., et al., 2014, *MNRAS*, 440, 2347
- Martocchia A., Matt G., 1996, *MNRAS*, 282, L53
- Miniutti G., Fabian A. C., 2004, *MNRAS*, 349, 1435
- Niedźwiecki A., Zdziarski A. A., 2018, *MNRAS*, in press, arXiv:1803.03781
- Niedźwiecki A., Życki P. T., 2008, *MNRAS*, 386, 759
- Niedźwiecki A., Zdziarski A. A., Szanecki M., 2016, *ApJ*, 821, L1
- Parker M. L., et al., 2014, *MNRAS*, 443, 1723
- Parker M. L., et al., 2015, *ApJ*, 808, 9
- Poutanen J., Svensson R., 1996, *ApJ*, 470, 249
- Reynolds C. S., Begelman M. C., 1997, *ApJ*, 488, 109
- Ross R. R., Fabian A. C., 1993, *MNRAS*, 261, 74
- Ross R. R., Fabian A. C., 2005, *MNRAS*, 358, 211
- Ross R. R., Fabian A. C., 2007, *MNRAS*, 381, 1697
- Tomsick J. A., et al., 2018, *ApJ*, 855, 3
- White T. R., Lightman A. P., Zdziarski A. A., 1988, *ApJ*, 331, 939
- Xu Y., et al., 2018, *ApJ*, 852, L34
- Zdziarski A. A., Gierliński M., 2004, *Prog. Theor. Phys. Suppl.*, 155, 99
- Zdziarski A. A., Grandi P., 2001, *ApJ*, 551, 186
- Zdziarski A. A., Johnson W. N., Magdziarz P., 1996, *MNRAS*, 283, 193
- Zdziarski A. A., Poutanen J., Johnson W. N., 2000, *ApJ*, 542, 703